



Stability of hydrous basaltic melts at low water fugacity: evidence for widespread melting at the lithosphere-asthenosphere boundary

Marija Putak Juriček^{1,2} · Hans Keppler¹

Received: 24 June 2024 / Accepted: 17 September 2024 / Published online: 7 October 2024
© The Author(s) 2024

Abstract

The upper mantle low velocity zone is often attributed to partial melting at the lithosphere-asthenosphere boundary. This implies that basaltic melts may be stable along plausible geotherms due to the freezing point depression in the presence of water and other incompatible impurities. However, the freezing point depression (ΔT) as a function of water content in the near-solidus basaltic melt (c_{H_2O}) cannot be precisely determined from peridotite melting experiments because of difficulties in recovering homogeneous basaltic glasses at high pressures. We therefore used an alternative approach to reinvestigate and accurately constrain the ΔT - c_{H_2O} relationship for basaltic melts at the low water fugacities that are expected in the upper mantle. Internally heated pressure vessel (IHPV) experiments were performed at water-saturated conditions in the anorthite-diopside- H_2O system at confining pressures of 0.02 to 0.2 GPa and temperatures between 940 and 1450 °C. We determined the water-saturated solidus, and obtained ΔT by combining our data with reports of dry melting temperatures in the anorthite-diopside system. In another series of experiments, we measured water solubility in haplobasaltic melts and extrapolated c_{H_2O} to pressures and temperatures of the water-saturated solidus. By combining the results from these two series of experiments, we showed that the effect of water on ΔT was previously underestimated by at least 50 °C. The new ΔT - c_{H_2O} relationship was then used to revise predictions of melt distribution in the upper mantle. Hydrous melt is almost certainly stable beneath extensive regions of the oceanic lithosphere, and may be present in younger and water-enriched zones of the subcontinental mantle.

Keywords Peridotite · Basalt · Lithosphere-asthenosphere boundary · Water · Melting · Cryoscopic equation

Introduction

Water is the most abundant volatile species in the Earth's upper mantle. Estimates from un-degassed MORB glasses and olivine-hosted melt inclusions from MORB indicate that 50 to 200 ppm of water is present throughout the upper mantle (Michael 1988, 1995; Danyushevsky et al. 2000; Saal et al. 2002). Similar water concentrations were observed in mantle xenoliths, ophiolites and abyssal peridotites

(Demouchy and Bolfan-Casanova 2016 and ref. therein), even though the water contents of those samples may have been modified during exhumation. At mantle pressures and at subsolidus conditions, water is accommodated mainly as OH^- point defects in nominally anhydrous minerals such as olivine and pyroxenes (e.g. Keppler and Bolfan-Casanova 2006; Mierdel et al. 2007). If the solidus temperatures are locally exceeded, however, water preferentially dissolves into the basaltic partial melts. Since the freezing point of liquids becomes depressed in the presence of solutes (e.g. Raoult 1882), these hydrous basaltic melts are stable at lower temperatures than their anhydrous analogues. Already some early experiments in the SiO_2 - H_2O system (Tuttle and England 1955) demonstrated that the effect of water on the freezing point depression of silicate liquids is significant, potentially exceeding hundreds of degrees. However, the freezing point of hydrous basaltic melts – or in other words, the melting point depression of peridotite in the presence of

Communicated by Dante Canil

✉ Hans Keppler
Hans.Keppler@uni-bayreuth.de

¹ Bayerisches Geoinstitut (BGI), Universität Bayreuth, 95440 Bayreuth, Germany

² Present address: Department of Mineralogy, Georg-August-Universität Göttingen, 37077 Göttingen, Germany

water – remains poorly quantified and the exact distribution of partial melt in the upper mantle is uncertain.

Accurate constraints on melt distribution in the upper mantle are of particular interest for understanding the origins of the lithosphere-asthenosphere boundary (LAB). Anderson and Sammis (1969) suggested that partial melting in the presence of water may be a viable explanation for the anomalously low seismic velocities and high attenuation in the upper mantle low velocity zone, and many recent seismological interpretations of the lithosphere-asthenosphere boundary also require the presence of partial melt (Rychert et al. 2020; Debayle et al. 2020; Hua et al. 2023). We note that a number of mechanisms that do not involve melting could at least partially account for the seismological observations. Some examples of the proposed sub-solidus mechanisms include contrasting rheological properties of dry and hydrated olivine (e.g. Karato and Jung 1998), grain-size variation effects (Faul and Jackson 2005), near-solidus seismic velocity reduction (Takei 2017) and differences in mantle oxidation state (Cline et al. 2018). However, the sharpness of the lithosphere-asthenosphere boundary (e.g. Rychert et al. 2020) would be hard to explain without invoking melting. While most studies focus on observations from seismic surveys, recent magnetotelluric imaging additionally characterized regions of high electrical conductivity in the upper mantle low velocity zone (Matsuno et al. 2010; Naif et al. 2013; Wang et al. 2020; Manassero et al. 2024), and these conductive regions are often more readily explained by partial melting, rather than being attributed to hydration of minerals.

Experimental studies of the partial melting of peridotite in the presence of just 50 to 200 ppm of water are technically impossible, because fine-grained silicates and oxides, which are used as starting materials in such studies, adsorb water when exposed to air. This atmospheric contamination in experimental samples may easily exceed the realistic mantle water abundances (Keppler and Rauch 2000). Moreover, the diffusion of hydrogen through the noble metal capsules commonly used in these experiments may further modify water contents, leading to large differences between nominal and real water contents in the charge. Experiments are more easily performed with high bulk water contents that allow measurements of melting temperatures and melt water contents, which can then be used to indirectly predict whether a peridotite will melt along plausible geotherms in the presence of realistically low water contents (Aubaud et al. 2004; Hirschmann et al. 2009; Tenner et al. 2012). However, such predictive models of hydrous peridotite melting are further hindered by difficulties in recovering homogeneous hydrous basaltic glasses from high pressures. In the short time required to quench the experimental samples, hydrous basaltic melts begin to crystallize and degas. While

high melt fractions quench into obvious dendritic crystals surrounded by silicate glass, low-degree near-solidus melts are not as easy to identify (Green 2015). One reason is that these melts may rapidly solidify by forming overgrowths on existing crystals during quenching. Moreover, at high pressures even the sub-solidus fluids will contain several wt% of dissolved silicate component, which may form interstitial quench products upon cooling. These quench phases may be visually very similar to former melt pools. For example, published estimates of the water-saturated solidus of peridotite vary by hundreds of degrees, from around 800 to 1100 °C at 3 GPa (e.g. Grove et al. 2006; Green 2015; Putak Juriček and Keppler 2023), which is likely a reflection of subjective textural discrimination between small melt pools and sub-solidus quench precipitates. Therefore, the melting point depression (ΔT) derived from experiments on hydrous peridotites may not be reliable. In addition to uncertainties in the observed ΔT , partial degassing and heterogeneous quench textures also preclude quantitative measurements of melt water contents (c_{H_2O}).

The relationship between the melting point depression (ΔT) and the near-solidus water content in basaltic melts (c_{H_2O}) is one of the essential experimental parameters for constraining melt distribution in the mantle. We therefore designed an approach that avoids most of the uncertainties inherent to experiments performed in the peridotite-H₂O system, which enabled us to precisely measure the ΔT - c_{H_2O} relationship for hydrous basaltic melts. Our approach is based on two essential concepts:

- (i) Instead of doing experiments in the peridotite system, we use the anorthite-diopside system to constrain the effect of water on the melting temperatures of basaltic melts. Anorthite-diopside is a eutectic system, where large amounts of melt are generated near the solidus, such that solidus temperatures can be very precisely determined. Moreover, the partial melts in the “haplobasaltic” anorthite-diopside system are very similar in bulk composition to natural basaltic melts, with the exception that Fe is replaced mostly by Ca. However, measurements of water solubility in basaltic melts show that water dissolution is rather insensitive to variations in bulk composition (e.g. Dixon et al. 1995; Shishkina et al. 2010; Lesne et al. 2011) and accordingly, this should have little effect on the relationship between water and melting point depression.
- (ii) Instead of trying to control water fugacity in high-pressure experiments by introducing water into the charge at the 100 ppm level – which is technically not feasible, as noted above – we simulate low water fugacities by performing melting experiments under water-saturated conditions, but at very low confining pressures. In such

experiments, water fugacity and melt water content can be precisely controlled.

We observed that formation of basaltic melts with water contents of 3 to 5 wt% is associated with melting point depressions of 150 to 200 °C – an effect that is notably larger compared to estimates from studies on hydrous peridotites (Katz et al. 2003; Hirschmann et al. 2009; Tenner et al. 2012). Our new ΔT - c_{H_2O} relationship significantly shifts the predictions of the current melting model for the upper mantle low velocity zone, suggesting the presence of low-degree melt along extensive regions in the uppermost asthenosphere.

Table 1 List of water-saturated melting experiments

| Melting experiments / An-Di mixture | | | | | |
|-------------------------------------|--------------------------------------|--------|-------------------|-----------------|---------------------|
| Run | P _{H₂O} (GPa) | T (°C) | Dura- tion (h) | Rapid quench | Phases ^a |
| ADS16 | 0.02 | 1150 | 8 | - | An, Di |
| ADS27 | 0.02 | 1200 | 24 | - | An, Di |
| ADS42 | 0.02 | 1207 | 24 | + | An, Di, melt |
| ADS37 | 0.02 | 1213 | 25 | + | An, Di, melt |
| ADS32 | 0.02 | 1225 | 24 | + | An, Di, melt |
| ADS15 | 0.02 | 1250 | 24 | + | An, melt |
| ADS18 | 0.05 | 1100 | 24 | + | An, Di |
| ADS17 | 0.05 | 1180 | 25 | + | An, Di |
| ADS43 | 0.05 | 1186 | 24 | + | An, Di, melt |
| ADS38 | 0.05 | 1192 | 31 | + | An, Di, melt |
| ADS33 | 0.05 | 1205 | 24 | + | An, Di, melt |
| ADS28 | 0.05 | 1230 | 24 | + | An, melt |
| ADS22 | 0.10 | 1040 | 46 | + | An, Di |
| ADS21 | 0.10 | 1120 | 25 | + | An, Di |
| ADS44 | 0.10 | 1128 | 24 | + | An, Di |
| ADS39 | 0.10 | 1135 | 24 | + | An, Di, melt |
| ADS34 | 0.10 | 1150 | 24 | + | An, Di, melt |
| ADS29 | 0.10 | 1180 | 24 | - | An, melt |
| ADS24 | 0.15 | 990 | 22 | + | An, Di |
| ADS23 | 0.15 | 1070 | 23 | + | An, Di |
| ADS35 | 0.15 | 1110 | 24 | + | An, Di |
| ADS45 | 0.15 | 1117 | 23 | + | An, Di |
| ADS40 | 0.15 | 1125 | 24 | + | An, Di, melt |
| ADS30 | 0.15 | 1140 | 24 | + | An, Di, melt |
| ADS26 | 0.20 | 940 | 25 | + | An, Di |
| ADS25 | 0.20 | 1020 | 72 | + | An, Di |
| ADS31 | 0.20 | 1100 | 24 | + | An, Di |
| ADS46 | 0.20 | 1107 | 27 | + | An, Di, melt |
| ADS41 | 0.20 | 1115 | 30 | + | An, Di, melt |
| ADS36 | 0.20 | 1130 | 24 | + | An, Di, melt |

^aAn additional hydrous fluid phase was present in all experiments. Rapid quench indicates whether the sample dropped into the cold zone of the autoclave (+) at the end of an experiment or not (-). P – pressure, T – temperature, An – anorthite, Di – diopside

Methods

General approach

Two series of experiments were performed in the anorthite-diopside-H₂O system at water-saturated conditions using a rapid-quench internally-heated pressure vessel (IHPV). The melt water contents and water fugacities were limited to suitably low values by maintaining low confining pressures (0.02 and 0.2 GPa). We first carried out melting experiments (Table 1) with a mixture of presynthesized high-purity anorthite and diopside in a 1:1 ratio (by weight) to determine the water-saturated melting temperatures (Fig. 1), which were easy to observe in this system, as a very high melt fraction is produced immediately at the solidus. Under water-saturated conditions the freezing point is defined by the dry and water-saturated solidi, so we combined our observations with literature reports of the dry melting temperatures in the anorthite-diopside system to obtain ΔT (Osborn 1942; Presnall et al. 1978).

The second series of experiments was performed to measure water solubility in the eutectic melts (Table 2). These experiments were carried out using mm-sized cylinders of haplobasaltic glass which had the eutectic melt composition in the anorthite diopside system, as reported by Osborn (1942) at 1 bar. The low pressures in our experiments also enabled recovery of homogeneous glasses, permitting accurate measurements of water solubility in this haplobasaltic melt as a function of pressure and temperature. The near-solidus melt water content (c_{H_2O}) was then obtained by extrapolating the water solubility values to the pressures and temperatures of the water-saturated solidus (Fig. 2).

Starting materials and experiments

For the synthesis of anorthite, stoichiometric amounts of Ca(OH)₂, Al(OH)₃ and SiO₂ were ground under ethanol in an agate mortar. The mixture was dehydrated in a platinum crucible by slow heating to 1100 °C, transferred to a high-temperature furnace, and then rapidly heated to 1600 °C. The melt was cooled to 1350 °C over four days. When the crucible was removed from the furnace, the content was still molten, despite being far below the equilibrium melting temperature. Placing the crucible on a cold surface caused nucleation of needle-like anorthite crystals at the bottom. The crucible was returned to the furnace at 1450 °C and cooled to 1350 °C over five hours. This yielded an aggregate of cm-sized elongated crystals. The purity of anorthite was confirmed by XRD. To synthesize diopside, a mixture of CaCO₃, Mg(OH)₂ and SiO₂ was homogenized in an agate mortar under ethanol. The mixture was sealed together with 10 wt% of distilled H₂O into several large gold capsules,

Fig. 1 (a) Summary of experiments. The melting experiments are denoted by circles; the dashed horizontal lines mark the solidus temperatures observed at each pressure. The water solubility experiments are shown as square symbols. (b) A literature compilation of solidus temperatures in the (nominally dry) anorthite-diopside and (water-saturated) anorthite-diopside-H₂O system. The dry solidus is after Osborn (1942) and Presnall et al. (1978), while the water-saturated solidus is defined by the datapoints from this study and from Yoder (1965). The dashed lines from (a) correspond to filled blue circles in (b)

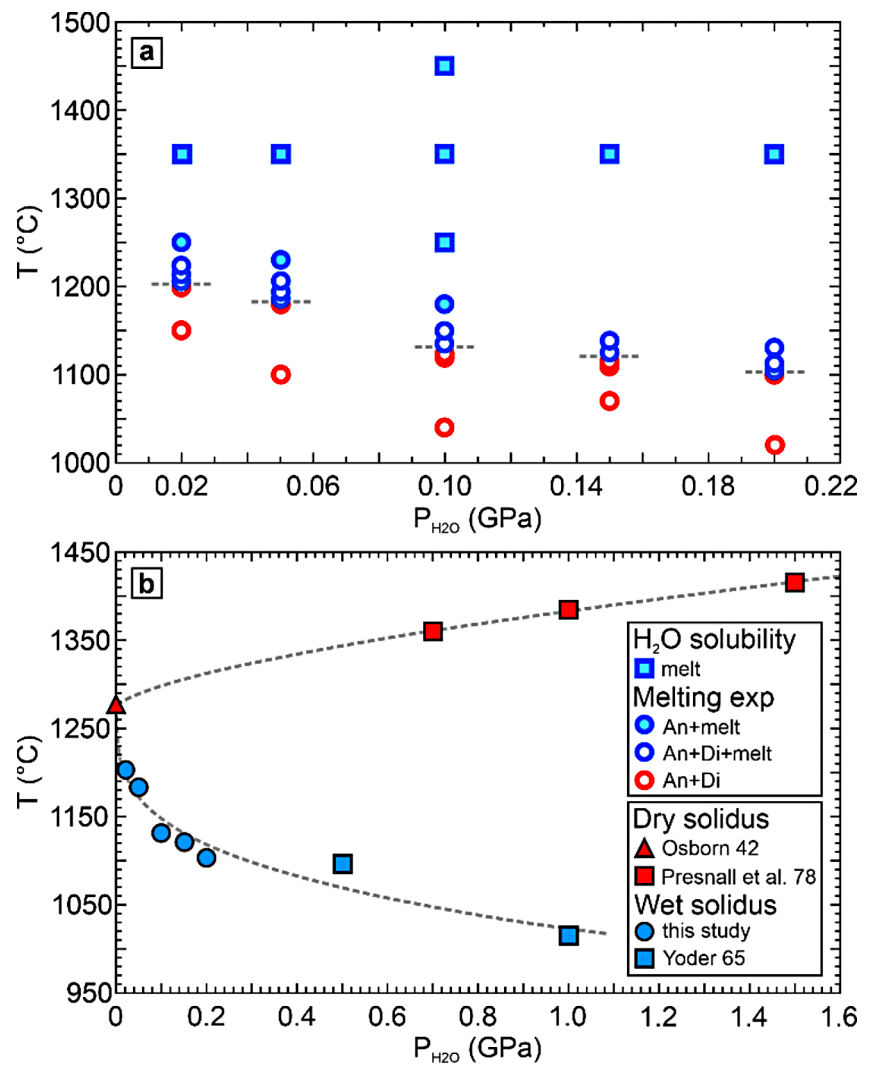
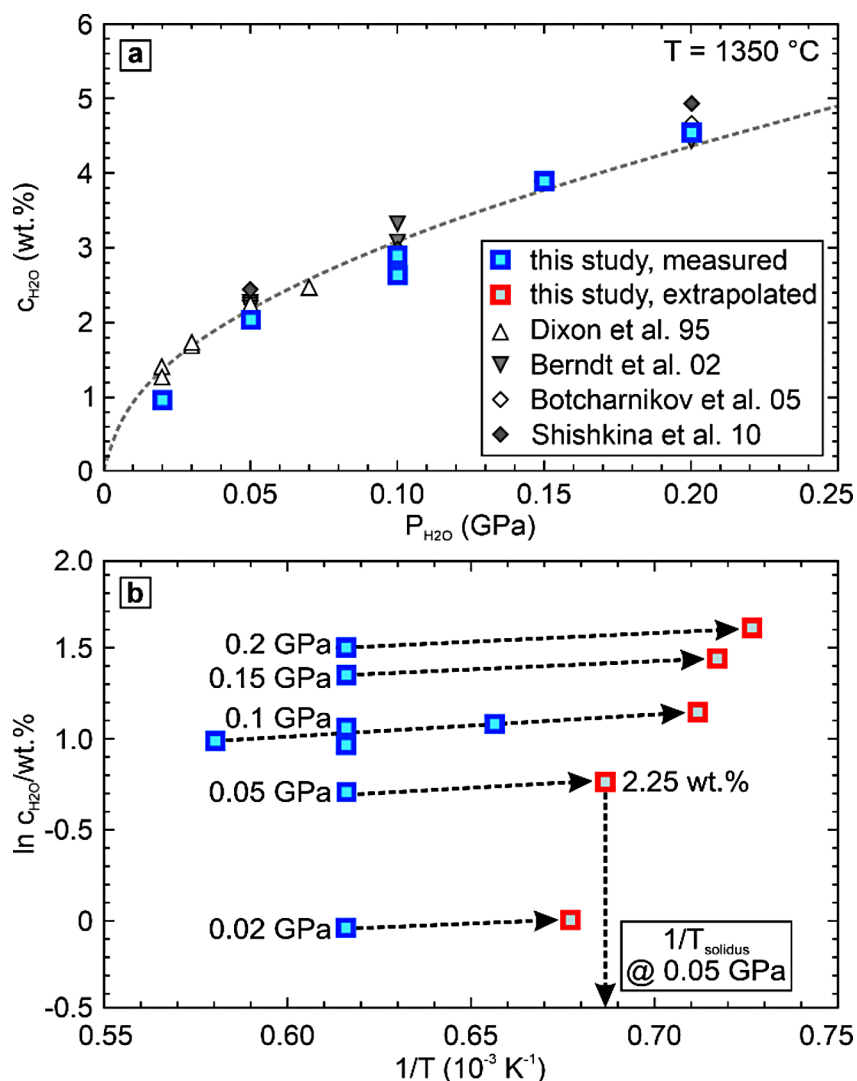


Table 2 List of water solubility experiments. Absolute water contents were determined from the weight difference in the recovered and dried run products (Fig. 2a). Sample 59 yielded an anomalously low value due to fluid entrapment in an isolated bubble. We obtained the molar adsorption coefficients for the near-infrared OH⁻ and H₂O bands in haplobasaltic glasses (Supplementary Information), and the values from FTIR measurements were extrapolated to the water-saturated solidus (Fig. 2b) and used in the model

| Run | P _{H₂O} (GPa) | T (°C) | H ₂ O solubility experiments / haplobasaltic glass | | | |
|-------|-----------------------------------|--------|---|--------|--|--|
| | | | Duration (h) | Quench | Weighing c _{H₂O} (wt%) | FTIR c _{H₂O} (wt%) |
| ADS56 | 0.02 | 1350 | 5 | + | 0.99 | 0.94 ± 0.05 |
| ADS57 | 0.05 | 1350 | 4 | + | 1.91 | 2.02 ± 0.10 |
| ADS58 | 0.1 | 1350 | 5 | - | 2.86 | 2.89 ± 0.13 |
| ADS59 | 0.15 | 1350 | 5 | + | --- | 3.88 ± 0.21 |
| ADS60 | 0.2 | 1350 | 5 | + | 4.44 | 4.53 ± 0.18 |
| ADS64 | 0.1 | 1250 | 5 | + | 2.89 | 2.96 ± 0.13 |
| ADS65 | 0.1 | 1350 | 5 | + | 2.76 | 2.62 ± 0.15 |
| ADS66 | 0.1 | 1450 | 5 | + | 2.77 | 2.68 ± 0.12 |

Plus and minus signs indicate whether rapid quench was successful (i.e. whether the sample dropped into the cold zone of the autoclave at the end of an experiment). P – pressure, T – temperature, “weighing c_{H₂O}” is the water content in the melt determined by mass balance from the weight loss of the capsule after piercing and drying, “FTIR c_{H₂O}” is the water content in the melt determined by FTIR measurements of the quenched glass. Standard deviation estimates are provided for “FTIR c_{H₂O}”

Fig. 2 (a) Pressure dependence of water solubility in haplobasalts from this study (at 1350 °C), compared to a literature compilation of water solubility in Fe-bearing tholeiitic basalts (at range of temperatures), including data from Dixon et al. (1995), Berndt et al. (2002), Botcharnikov et al. (2005), and Shishkina et al. (2010). (b) Extrapolation of melt water content (using Eq. 2) to the experimentally observed solidus temperatures. Blue symbols show the experimental measurements, corresponding to the blue squares from Fig. 1a. The red symbols are the extrapolated values, which are provided in Table 3



which were kept at 3 kbar and 700 °C for approximately 10 days in externally heated cold-seal pressure vessels. The run products were analysed by XRD, revealing minor carbonate impurities. The carbonates were dissolved by treating the powders with 10% HNO₃ for an hour at room temperature. Nitric acid was removed by washing with distilled H₂O and subsequent drying. The purity of diopside was checked again using XRD. The typical crystal size was 5–10 μm. The haplobasaltic glass was synthesized from high-purity CaCO₃, Al(OH)₃, Mg(OH)₂ and SiO₂, which were mixed in an agate mortar under ethanol, and then decarbonated and dehydrated at 1100 °C for 12 h. This yielded a stoichiometry of An₄₁Di₅₉ (wt%), as reported previously by Osborn (1942). The sintered material was melted at 1400 °C for 2 h, and the glass was formed by cooling in air.

The starting materials were arc-sealed together with distilled H₂O into 2 cm long platinum capsules with 3.5/3.2 mm outer/inner diameter. The experiments were performed in a vertically-oriented internally-heated gas pressure vessel

made by Harwood Engineering, Walpole, MA, USA. Argon was used as pressure medium, and pressure was measured with a Harwood manganin cell. The temperature was monitored by two S-type thermocouples, coupled to Eurotherm devices which separately controlled the power supply to the two furnace windings. The samples were suspended on a Pt wire between the thermocouples, with temperatures and pressures maintained within ± 2 °C and ± 5 MPa, with respect to values reported in Tables 1 and 2. The experiments were terminated with an isobaric rapid quench by fusing the wire which held the capsule, dropping the sample into the cold zone of the autoclave (e.g. Berndt et al. 2002). Success of the quench was evaluated based on the 1–5 bar pressure increase upon fusing the quench wire, and/or by the sample location in the cold spot after opening the vessel. All samples were dried at 150 °C after the experiments, pierced with a steel needle, then dried again and weighed. The presence of excess water after the run was confirmed by weight loss after piercing and drying.

Analytical methods

The run products from melting experiments were examined using a ZEISS-LEO 1530 Gemini SEM, and we characterized the composition of some eutectic melt pools with a JEOL JXA-8200 electron microprobe (Supplementary Information). The water contents in haplobasaltic cylinders were determined using Fourier-transform infrared spectroscopy (FTIR). The infrared spectra were measured with a Bruker IFS 120 Fourier-transform infrared spectrometer, coupled to an all-reflecting Bruker IRscope I microscope. The instrument contains a permanently aligned Michelson-type interferometer with a 30° angle of incidence on the beamsplitter. Mirror retardation is monitored with a frequency stabilized HeNe laser, and the instrument optic system is evacuated. All measurements were performed with a tungsten light source, a Si-coated CaF₂ beam-splitter and a narrow-band mercury cadmium telluride (MCT) detector. Two hundred scans were accumulated per spectra, with 1 cm⁻¹ resolution. The spectra were obtained from mm-sized glass fragments, doubly-polished to approximately 285–300 μm thickness. Molar absorption coefficients for the 4500 cm⁻¹ and 5200 cm⁻¹ bands of OH⁻ and H₂O were calibrated against water loss in the recovered and dried samples (Supplementary Information; e.g. Ohlhorst et al. 2001; Shishkina et al. 2010). Water solubility experiments were performed above the liquidus temperatures and the recovered glasses were almost always bubble-free. As the glass cylinders have a small surface area that limited contamination with atmospheric water (Keppler and Rauch 2000), and only minor weight losses during welding were tolerated (< 2 wt% of nominal water content), the total amounts of water in the run charges were reliably known.

Results

The hydrous solidus was defined by the first appearance of melt pools that coexisted with both anorthite and diopside in a narrow temperature range of about 20 °C (Fig. 1a; Supplementary Information, Fig. S1b). The eutectic temperatures observed in our study, along with reports from previous

studies in the anorthite-diopside and anorthite-diopside-H₂O systems (Osborn 1942; Yoder 1965; Presnall et al. 1978), define the melting point depression ΔT (Fig. 1b).

The calibration of molar absorption coefficients yielded values of 0.58 ± 0.03 and 0.55 ± 0.03 L mol⁻¹ cm⁻¹ for the OH⁻ and H₂O bands in haplobasaltic glasses, respectively (Supplementary Information). We note that these linear extinction coefficients are similar to, but slightly smaller than the data reported by Shishkina et al. (2010) for tholeiitic glasses. The results of water-solubility measurements are provided in Table 2, and the extrapolation of water contents to near-solidus conditions (Table 3) was carried out using the values that were derived from FTIR measurements. Water solubility in silicate melts increases with the square root of water fugacity in the pressure range of interest and at temperatures above 1000 °C, where $f_{\text{H}_2\text{O}} \approx$ confining pressure. Therefore, the water solubility measurements from the experiments at constant temperature (1350 °C) can be fitted to a square root function as:

$$c_{\text{H}_2\text{O}} = a P^{0.5} \quad (1)$$

where P is pressure [GPa], a is an experimentally derived parameter, and $c_{\text{H}_2\text{O}}$ is the total water concentration [wt%] measured in the glasses by FTIR. Fitting our data obtained at a constant temperature of 1350 °C (Fig. 1a) to Eq. 1 yields a value of 9.743 for the parameter a with a residual standard error of ± 0.31 wt% and an $R^2 = 0.981$ (Fig. 2a). Figure 2a also shows that the water solubility data obtained in our “haplobasaltic” model system are nearly indistinguishable from those measured for various Fe-bearing basalt compositions. This confirms our assumption that the behaviour of water in the anorthite-diopside-H₂O system is an excellent model for the effect of water on the melting point of basalts in general.

The effect of temperature on water solubility in silicate melts is almost negligible and can be described at constant pressure as:

$$\ln \frac{c_{\text{H}_2\text{O}}}{[\text{wt.}\%]} = b + c \frac{10^3}{T} \quad (2)$$

Table 3 Compositions of eutectic melts from this study

| P (GPa) | An (wt%) ^b | Wet solidus (°C) | ΔT (°C) | SiO ₂ | Al ₂ O ₃ | CaO | MgO | H ₂ O ^a |
|-----------|-----------------------|------------------|-----------------|------------------|--------------------------------|-------|------|-------------------------------|
| 0.02 | 47 | 1203 | 80 | 49.14 | 17.03 | 22.93 | 9.75 | 1.15 |
| 0.05 | 50 | 1183 | 107 | 48.23 | 17.91 | 22.51 | 9.10 | 2.25 |
| 0.1 | 54 | 1131 | 167 | 47.34 | 19.18 | 22.09 | 8.30 | 3.09 |
| 0.15 | 56 | 1121 | 185 | 46.56 | 19.66 | 21.73 | 7.85 | 4.20 |
| 0.2 | 59 | 1103 | 209 | 45.89 | 20.57 | 21.41 | 7.26 | 4.87 |

^aWater contents in the melt are obtained by extrapolation of values obtained by FTIR measurements (Eqs. 1 and 2; Fig. 2b). ^bMelt compositions, expressed as the proportion of the anorthite component (wt%) on anhydrous basis, are interpolated from literature data (Osborn 1942; Yoder 1965) and our EPMA analyses at 0.2 GPa (Supplementary Information). All compositions are given in wt%. The residual standard errors are ± 3 wt% for the proportion of An in the melt, and ± 16 °C for the wet solidus and for the ΔT (Supplementary Information)

where T is absolute temperature [K], and b and c are experimentally derived parameters. At a constant pressure of 0.1 GPa, we obtained values of 0.221 and 1.301 for parameters b and c ($R^2=0.497$), respectively. The residual standard error of Eq. 2 is ± 0.15 wt%, expressed in terms of c_{H_2O} . The dc_{H_2O}/dT was assumed to be independent of pressure. Equation 2 was used to extrapolate the water concentrations in the melt to the experimentally observed solidus temperatures (Fig. 2b). The extrapolated water concentrations are provided in Table 3, along with the corresponding melt compositions and melting point depressions. Combining the results from both series of experiments demonstrates that the melting point is lowered by more than 200 °C at 0.2 GPa, and the melt water content corresponding to this ΔT is 4.87 wt% (Table 3). We then used some of our microprobe measurements together with literature data (Osborn 1942; Yoder 1965) to obtain the compositions of near-solidus melts in terms of the anorthite component (Table 3; Supplementary Information).

Discussion

Melting point depression in basaltic (silicate-H₂O) systems

The melting point in magmatic systems can be described by the cryoscopic equation (e.g. Aubaud et al. 2004; Hirschmann et al. 2009; Tenner et al. 2012). Assuming ideal mixing between water and the silicate component in the melt, the equilibrium condition at the hydrous solidus is:

$$G_s = G_l + RT \ln X_{\text{silicate}} \quad (3)$$

where G_s and G_l are the Gibbs free energies of pure silicate solid(s) and pure silicate liquid, R is the ideal gas constant, T is absolute temperature and X_{silicate} is the mole fraction of the silicate component in the hydrous liquid phase. Equation (3) can be rearranged:

$$\frac{G_s - G_l}{RT} = \ln X_{\text{silicate}} \quad (4)$$

Differentiating Eq. (4) with respect to temperature, and using the Gibbs-Helmholtz equation to solve the left-hand side of the expression, one obtains:

$$\frac{H_l - H_s}{RT^2} = \frac{\Delta H_{\text{fus, dry}}}{RT^2} = \frac{d \ln X_{\text{silicate}}}{dT} \quad (5)$$

where H_s and H_l are the enthalpies of pure silicate solid(s) and pure silicate liquid, and $\Delta H_{\text{fus, dry}}$ is the enthalpy of fusion of the dry system (Supplementary Information; Richet and Bottinga 1984; Lange et al. 1991; De Yoreo et

al. 1995). Equation (5) can be integrated between the limits for pure silicate ($X_{\text{silicate}}=1$, $T=T_{\text{dry}}$) and the silicate-H₂O system (X_{silicate} , T):

$$\frac{\Delta H_{\text{fus, dry}}}{R} \int_{T_{\text{dry}}}^T \frac{dT}{T^2} = \int_1^{X_{\text{silicate}}} d \ln X_{\text{silicate}} \quad (6)$$

where T_{dry} is the solidus temperature of the dry system, and T is the solidus temperature of the silicate-H₂O system at a given X_{silicate} . Assuming that $\Delta H_{\text{fus, dry}}$ remains constant between T_{dry} and T , integration of (6) yields the cryoscopic equation:

$$\frac{\Delta H_{\text{fus, dry}}}{R} \left(\frac{1}{T_{\text{dry}}} - \frac{1}{T} \right) = \ln X_{\text{silicate}} \quad (7)$$

Water dissolution in silicate liquids is governed by reaction (8), where H_2O_{melt} and OH^-_{melt} are the water species dissolved in the melt, and O_{melt} are the bridging oxygen atoms in the silicate melt network. This reaction was initially proposed by Bartholomew et al. (1980) and Stolper (1982), and later confirmed by in-situ FTIR spectroscopic studies of water speciation in haplogranitic melts (Nowak and Behrens 1995; Shen and Keppler 1995).



In-situ studies showed that the equilibrium constant for reaction (8) is influenced by temperature, but the water speciation (at constant water content in the melt) is not significantly pressure dependent. Both studies noted that the equilibrium of reaction (8) is strongly shifted to the right at high temperatures, and that water speciation is modified upon cooling, even when the melt is rapidly quenched. We therefore expect that our quenched haplobasaltic glasses do not preserve the water speciation they had at run conditions. This presents a challenge, as the X_{silicate} required by Eq. (7) is:

$$X_{\text{silicate}} = 1 - X_{H_2O} - X_{OH} \quad (9)$$

where X_{H_2O} and X_{OH} are the mole fractions of the respective water species in the melt *at run conditions*. The X_{H_2O} and X_{OH} could theoretically be estimated from the equilibrium constant of reaction (8) and from the total water concentration in the quenched glasses (c_{H_2O}), except that no in-situ measurements of water speciation at high temperatures are available for basaltic melts. Another ambiguity in defining X_{silicate} is the formulation of a silicate molar unit. How many oxygen atoms should be assigned to a single molar unit to describe the average lifetime of shortrange ordering in a silicate liquid at high temperature?

Parametrization 1: Defining the silicate molar unit

The cryoscopic Eq. (7) implies that the relationship between $\ln X_{\text{silicate}}$ and $1/T$ should be linear:

$$\ln X_{\text{silicate}} = d + e \frac{1}{T} \quad (10)$$

where d and e are experimentally derived parameters. To find the proper definition of a silicate molar unit, we begin with a simplified model that assumes complete dissociation of water in the melt into hydroxyl groups. At the high temperatures and low total water concentrations of our experiments, hydroxyl groups are expected to be the dominant species (e.g. Nowak and Behrens 1995; Shen and Keppler 1995), and this assumption is a good first approximation. We obtained the molar weights of silicate units calculated on 1-, 3-, 4- and 8-oxygen basis from the known near-solidus melt compositions (Table 3), and estimated the $X_{\text{H}_2\text{O}, \text{total}}$. The $X_{\text{H}_2\text{O}, \text{total}}$ is the mole fraction of the total water content in haplobasaltic glasses, measured by FTIR and expressed as molecular water. According to the assumptions of Parametrization 1, one mole of water measured in the glass phase corresponds to two moles of hydroxyl groups in the melt at run conditions:

$$X_{\text{OH}} = 2X_{\text{H}_2\text{O}, \text{total}} \quad (11)$$

and X_{silicate} can be estimated (Eq. 12). The experimentally observed hydrous melting temperatures ($1/T$) were plotted against sets of X_{silicate} values that were derived by assuming 1-, 3-, 4- and 8-oxygen silicate molar units. The parameters d and e were obtained by linear regression, and the results of Parametrization 1 are summarized in Table 4. The fit of $\ln X_{\text{silicate}} - 1/T$ plot to a linear function gradually deteriorates with increasing molar weight of the silicate unit. Moreover, for large molar units the dry melting temperature (Osborn 1942) deviates from the trend that is defined by the hydrous melting temperatures (see Fig. 3). The most accurate prediction of the dry melting point is obtained by assuming a 1-oxygen molar unit, and it is within 25 °C of the experimental observation (Osborn 1942).

$$X_{\text{silicate}} = 1 - X_{\text{OH}} \quad (12)$$

This suggests that the silicate melt structure is best approximated with a small 1-oxygen molar unit, and that the existence of large polymer-like units that contain many bridging oxygens is unlikely at magmatic temperatures. Our result is overall consistent with insitu ^{29}Si NMR spectroscopic observations of silicate liquids, as Stebbins (1995) described rapid exchange of Si atoms between different coordination sites within the melt structure already several hundreds of degrees above the glass transition temperature range.

Parametrization 2: Introducing water speciation

The 1-oxygen silicate unit is used throughout Parametrization 2, where we consider that water speciation at run conditions is governed by a temperature-dependent reaction (8). The equilibrium constant for reaction (8) can be written as:

$$K = \frac{(X_{\text{OH}})^2}{X_{\text{H}_2\text{O}}} \quad (13)$$

where the notation is the same as before, and the relationship between $X_{\text{H}_2\text{O}, \text{total}}$, $X_{\text{H}_2\text{O}}$ and X_{OH} is given by Eq. (14). Then for some equilibrium constant K , Eqs. (13) and (14) can be solved for $X_{\text{H}_2\text{O}}$ and X_{OH} , and for the corresponding X_{silicate} (9).

$$X_{\text{H}_2\text{O}, \text{total}} = X_{\text{H}_2\text{O}} + \frac{1}{2}X_{\text{OH}} \quad (14)$$

The equilibrium constant can be described as (Nowak and Behrens 1995; Shen and Keppler 1995):

$$\ln K = f + g \frac{1}{T} \quad (15)$$

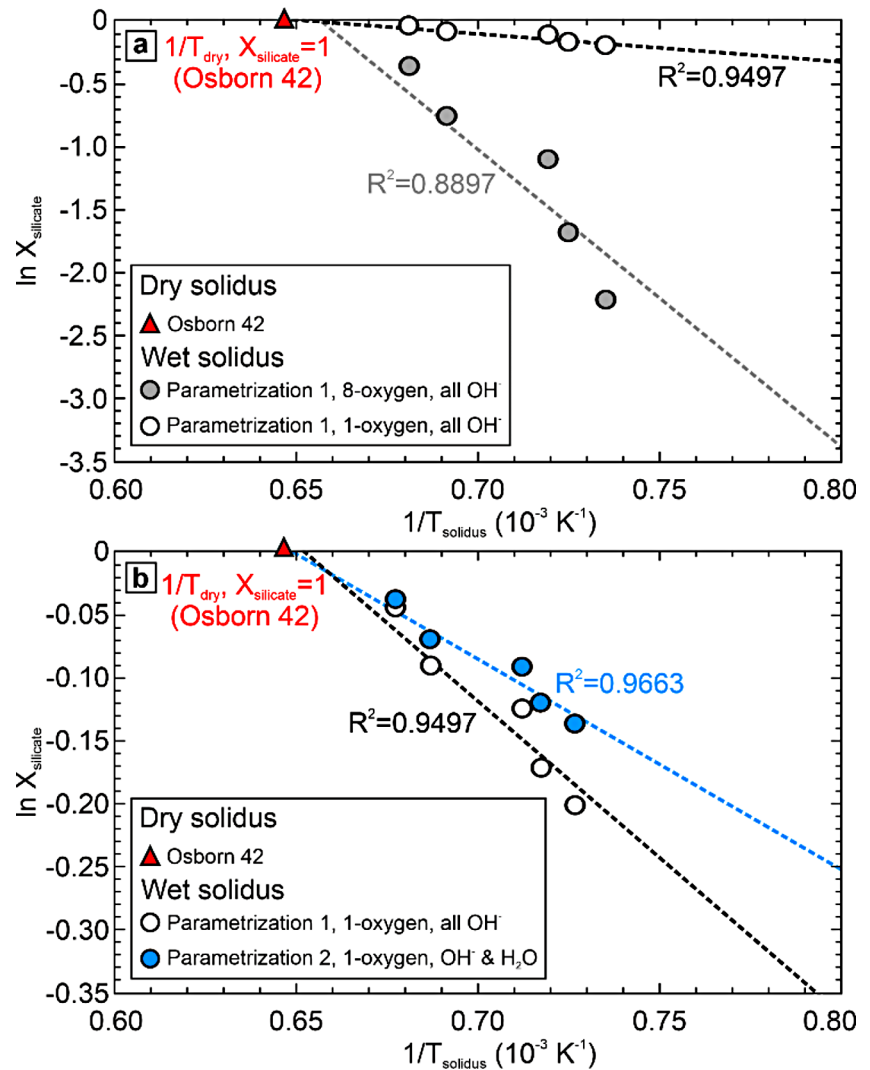
$$f = \frac{\Delta S^0}{R} \quad (16)$$

$$g = -\frac{\Delta H^0}{R} \quad (17)$$

Table 4 The freezing point depression of hydrous basaltic melts. Parametrization 1 assumes different silicate molar units and complete dissociation of water in the melt as OH^- groups (Fig. 3a). Parametrization 2 tests different temperature-dependent equilibrium constants for the water speciation reaction (Eq. 8); the best-fit silicate molar unit (1-oxygen) from Parametrization 1 is assumed. ^aValues based on the in-situ studies of water speciation in haplogranitic melts (Nowak and Behrens 1995; Shen and Keppler 1995). ^bOne example of a best-fit to the data from this study; for a complete summary of Parametrization 2 see the Supplementary Information (table S1)

| Parametrization | Silicate unit | H ₂ O species | d | e | f | g | R ² |
|-----------------|----------------------|------------------------------------|--------|---------|-------|---------|----------------|
| 1 | 8-oxygen (283 g/mol) | all OH ⁻ | 16.919 | -25 834 | - | - | 0.8897 |
| 1 | 4-oxygen (141 g/mol) | all OH ⁻ | 6.744 | -10 342 | - | - | 0.9418 |
| 1 | 3-oxygen (106 g/mol) | all OH ⁻ | 4.938 | -7577 | - | - | 0.9458 |
| 1 | 1-oxygen (35 g/mol) | all OH ⁻ | 1.604 | -2462 | - | - | 0.9497 |
| 2 ^a | 1-oxygen (35 g/mol) | OH ⁻ & H ₂ O | 1.084 | -1671 | 0.58 | -4000 | 0.9663 |
| 2 ^b | 1-oxygen (35 g/mol) | OH ⁻ & H ₂ O | 1.047 | -1617 | 12.65 | -21,000 | 0.9676 |

Fig. 3 The $\ln X_{\text{silicate}} - 1/T$ plots for different parametrizations of the freezing point depression. The plots test the linear relationship between $\ln X_{\text{silicate}}$ and $1/T$, which is predicted by Eq. (7). **(a)** Comparison of models that assume 8-oxygen and 1-oxygen silicate molar units, with complete dissociation of water to OH^- groups at run conditions (Parametrization 1 from Table 4). Smaller silicate molar units are more consistent with theoretical predictions. **(b)** Comparison of Parametrization 1 (complete dissociation of water to OH^-) and Parametrization 2 (dissolution of water as both OH^- and molecular H_2O) for the best-fit silicate molar unit (1-oxygen). Introducing water speciation improves the fit of $\ln X_{\text{silicate}} - 1/T$ to a straight line. Note that the dashed black lines in both **(a)** and **(b)** are the same fit ($d = 1.604$, $e = -2462$), but the y-axis scaling is different. The dashed blue line in **(b)** corresponds to Parametrization 2^a from Table 4



where parameters f and g are derived experimentally, and ΔS^0 and ΔH^0 are the standard state entropy and enthalpy of the water speciation reaction in the silicate melt. Since no in-situ measurements of K are available for basaltic melts, for some chosen g , the y-axis intercept f was adjusted to yield $X_{\text{H}_2\text{O}}$, X_{OH} and X_{silicate} that result in a best-fit of the $\ln X_{\text{silicate}} - 1/T$ plot to a straight line. We calculated the equilibrium constants, and generated the $\ln X_{\text{silicate}} - 1/T$ plots, for a wide range of parameter g values.

As expected, the fit of $\ln X_{\text{silicate}} - 1/T$ to a linear function improved further, from $R^2 = 0.9497$ in Parametrization 1 to $0.96 < R^2 < 0.97$ in Parametrization 2, after introducing a temperature dependent equilibrium constant for the water speciation reaction in the melt phase. The standard state enthalpy for the water speciation reaction in the melt phase (Eq. 17) that was obtained by Shen and Keppler (1995) is very similar to the value reported by Nowak and Behrens (1995), despite the significantly higher alkali and lower silica content of the melt from the latter study. It was suggested

that ΔH^0 may be fairly insensitive to the bulk composition of the silicate liquid. In addition, the water speciation in quenched silicate glasses is similar across the range of natural magmatic compositions (Stolper 1982). We therefore began by assuming a parameter g that is based on the previous in-situ measurements in haplogranitic melts, and the results of this calculation are given in Table 4 as Parametrization 2^a. The value of g was then gradually increased until the fit to Eq. (10) began to deteriorate. However, a similar goodness-of-fit was obtained for a range of g values, such that the temperature dependence of the equilibrium constant K could not be entirely constrained for basaltic melts. The Parametrization 2^b from Table 4 is one example of a set of values for parameters d , e , f and g that yielded a best-fit to Eq. (10). Results of Parametrization 2 are provided in the Supplementary Information (Table S1), where all of the best-fit values for parameter g are given, together with their corresponding values of d , e and f . We note that Parametrizations 2^a and 2^b predict the dry melting temperature quite

accurately – within 6 and 1 °C of the value reported by Osborn (1942), respectively.

In Fig. 4, the new parametrization of the freezing point depression for hydrous basaltic melts is compared to published ΔT - c_{H_2O} models, which were calibrated against experimental studies on partial melting of peridotites at pressures above 1 GPa (Katz et al. 2003; Hirschmann et al. 2009; Tenner et al. 2012). Our data suggest that melt water contents of several wt% may be associated with ΔT that are higher by around 50 °C, with respect to models from previous studies (Fig. 4). Our Parametrizations 2^a and 2^b were then used to extrapolate the ΔT - c_{H_2O} relationship to melt water contents that exceed the range of experimental observation. Extrapolation to higher melt water contents resulted in an even larger divergence from the previous ΔT - c_{H_2O} estimates (Fig. 4). While the data obtained in the anorthite-diopside-H₂O system plot above the trend defined by hydrous peridotites, we do note that many of the peridotite datapoints – particularly those from experiments performed at 1 to 3 GPa – agree with our observation. The divergence from previous estimates likely arises due to the considerable

scatter in the hydrous peridotite data, which may be related to the difficulty in detecting small fractions of partial melt in such experiments. Naturally, this will cause some systematic under-estimation of the actual melting point depression induced by water.

In addition to the formal parametrization that is discussed above, Katz et al. (2003) proposed to describe the ΔT - c_{H_2O} relationship by an empirical power law function:

$$\Delta T = h(c_{H_2O})^i \quad (18)$$

where the melt water content is given directly in wt%, and h and i are determined from the best-fit to experimental data. Katz et al. (2003) report values of 43 and 0.75 for the parameters h and i , based on a subset of the hydrous peridotite dataset (Fig. 4). This type of equation can describe our dataset as well, using an exponent value of $i=0.75$ and $h=67.8$ ($R^2 > 0.98$). This approach may be preferred for approximating the ΔT - c_{H_2O} relationship due to its simplicity, even though it has no theoretical foundation. We emphasize that for higher melt water contents, which are relevant

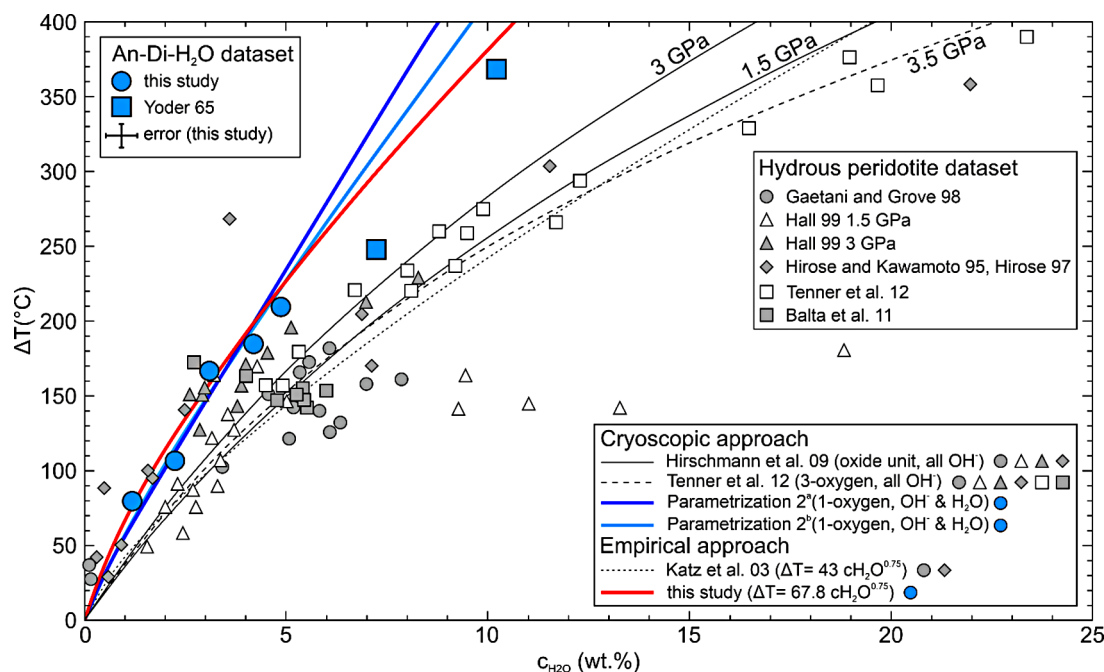


Fig. 4 Comparison of different parametrizations for the ΔT - c_{H_2O} relationship. The hydrous peridotite dataset is shown as white and grey symbols, and it is based on previous literature compilations (Katz et al. 2003; Hirschmann et al. 2009; Tenner et al. 2012), including data from Gaetani and Grove (1998), Hall (1999), Hirose and Kawamoto (1995), Hirose (1997), and Balta et al. (2011). The anorthite-diopside-H₂O dataset consists mostly of our own data. Two additional datapoints (blue squares) were obtained by combining eutectic temperatures reported by Yoder (1965) with melt water contents that were extrapolated from our water solubility measurements. Note that the data from Yoder (1965) are not used for the new ΔT - c_{H_2O} parametrizations. The water contents corresponding to solidus temperatures at 0.5 and 1 GPa were not directly measured, and attempts to include the additional

datapoints to Parametrization 2 resulted in a poorer fit of $\ln X_{\text{silicate}} - 1/T$ to a straight line. The error bars in the legend (top left corner) are estimates of the residual standard errors in our dataset (± 0.4 wt% c_{H_2O} and ± 16 °C ΔT). Literature compilations that were used for each of the ΔT - c_{H_2O} estimates are indicated by symbols in the legend (lower right corner). The entire anorthite-diopside-H₂O dataset plots above the trend defined by hydrous peridotites. The previous estimates of ΔT - c_{H_2O} relationship are shown as thin black lines, and the updated parametrizations are highlighted by the bold blue and red lines. Parametrizations 2^a and 2^b (Table 4) constrain the ΔT - c_{H_2O} relationship for higher melt water contents (dark and light blue lines). The empirical power law fit, proposed by Katz et al. (2003), but recalibrated with our data, is also plotted (red line)

for predicting partial melting in the subcontinental mantle (Supplementary Information, Fig. S5), the new power law fit deviates from Parametrization 2, although not nearly as much as the estimates from previous studies (Fig. 4). For c_{H_2O} greater than about 6 wt%, we recommend the use of Parametrization 2.

The cryoscopic approach described here essentially considers the entropy effect of the dissolution of water in the silicate melt on the melting point depression. However, the dissolution of water in the melt also influences the volume change ΔV upon melting. The magnitude and direction of this effect depends on the partial molar volumes of water V_{H_2O} in the silicate melt and in nominally anhydrous minerals. V_{H_2O} in olivine and orthopyroxene can be derived from a thermodynamic analysis of the pressure dependence of water solubility. This yields values in the range of 10–12 cm³/mol for both minerals (Keppler and Bolfan-Casanova 2006). The partial molar volume of water in silicate melts strongly depends on pressure, and to a lesser extent, on temperature. It decreases from > 20 cm³/mol at 1 bar to about 5 cm³/mol at 25 GPa (Sakamaki et al. 2009 and references therein). Conveniently, in the range of 3–5 GPa, which is most relevant for the seismic low velocity zone, V_{H_2O} in the melt approaches values of 10–12 cm³/mol, such that there is almost no volume change associated with the dissolution of water in the silicate melt and correspondingly, little additional effect on the melting point depression. At higher pressure, the melting point depression would be increased beyond that inferred from the purely cryoscopic approach, while at lower pressures, it would be decreased. Some rough thermodynamic estimates suggest that in the pressure range relevant for the seismic low velocity zone, this effect will never exceed 10% of the inferred ΔT .

Melting in the seismic low velocity zone

The new ΔT - c_{H_2O} parametrization for basaltic melts was used to revisit the predictions of hydrous partial melting in the low velocity zone of the upper mantle (Hirschmann et al. 2009). We note that the mantle also contains variable amounts of carbon (e.g. Le Voyer et al. 2017), which is likely stored in the form of carbonates at sub-solidus conditions (Canil 1990; Shcheka et al. 2006), but upon melting contributes an additional freezing point depression due to dissolution of CO₂ in the carbonatitic-silicate liquids (e.g. Hirschmann 2010). Due to the small abundance of carbon in the normal MORB-source mantle (Saal et al. 2002), the possible fraction of carbonatite melt should be restricted to less than 0.1 wt%, which is likely insufficient to explain the reduced seismic velocities near the LAB. This suggests that the melts near the LAB are basaltic *sensu lato*, and our parametrization is applicable. However, as the model

considers the isolated effect of water on the melting point depression of peridotite, the extent of partial melting predicted here is likely a conservative estimate. In principle, the stability of hydrous melts may be calculated using the following procedure:

- (i) From the published mineral/melt partition coefficients for water, one may calculate the water content in a partial melt for a given bulk water content in the mantle, pressure, temperature, and degree of melting.
- (ii) Using our newly calibrated ΔT - c_{H_2O} parametrization, one can then predict how much the solidus of this melt would be depressed, relative to the dry peridotite solidus.
- (iii) The predicted melting point depression can be compared to the temperature difference between the geotherm and the dry peridotite solidus at a given depth in the mantle. If the melting point depression is larger than this temperature difference, hydrous melt will be present in the mantle at this depth.

The results of such calculations along typical oceanic geotherms, using various assumptions, are compiled in Fig. 5. The uncertainty in our experimental data may have a small effect on model predictions, plausibly shifting the bulk water contents required for melting by up to 20–30 ppm. Further uncertainties arise because the hydrous melting model requires the knowledge of geothermal gradients, of the dry peridotite solidus temperatures, and of the olivine/melt and pyroxene/melt partition coefficients for water (see Supplementary Information and Hirschmann et al. 2009). The mineral/melt partition coefficients are dependent on pressure, temperature and water activity in the mantle (Keppler and Bolfan-Casanova 2006). The melting model proposed by Hirschmann et al. (2009) attempts to capture the pressure dependence of water partitioning between mantle minerals and melts, but omits the possible effects of temperature and water activity. Moreover, the published mineral/melt partition coefficients vary considerably, which may be related to analytical uncertainties in both mineral and melt analyses (Koga et al. 2003; Aubaud et al. 2004, 2008; Smyth et al. 2006; Hauri et al. 2006; Litasov et al. 2007; Grant et al. 2007; Bali et al. 2008; Withers and Hirschmann 2008; Tenner et al. 2009; Dobson et al. 1995; O’Leary et al. 2010; Le Voyer et al. 2014; Adam et al. 2016; Newcombe et al. 2020). Because of the wide range of published mineral/melt partition coefficient values, in the Supplementary Information we argue that even their pressure dependence can be arbitrarily described by different mathematical expressions. This introduces uncertainties to the model predictions, shifting the bulk water content required for melting by at least 50 ppm. All other parameters being equal, in Fig. 5a and b we

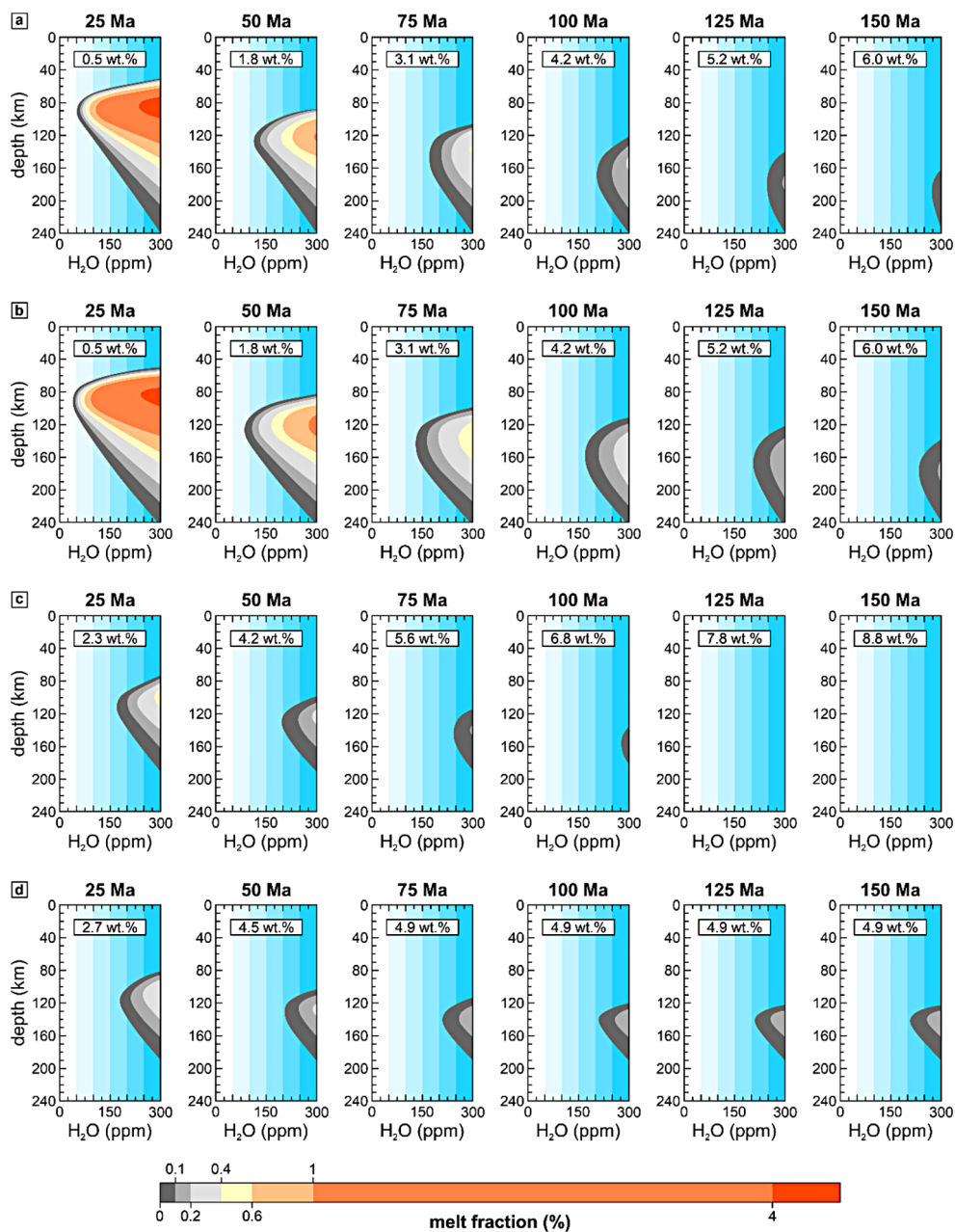


Fig. 5 Predictions of hydrous partial melting along the oceanic lithosphere-asthenosphere boundary as a function of plate age. The y-axes are depth, the x-axes are assumed bulk mantle water contents. The values inside the panels are the c_{H_2O} in the incipient melt, corresponding to the lowest bulk water content for which melting is predicted. All panels were generated using the dry peridotite solidus after Walter (1998) and the updated ΔT - c_{H_2O} relationship (the empirical power law relationship). However, we explored different mineral/melt partition coefficients for water and a range of thermal models. **(a)** We assumed the thermal structure of the oceanic lithosphere described by the half-space cooling model (e.g. Schubert et al. 2001) with 10 °C seafloor temperature (Hua et al. 2023), thermal diffusivity of 0.8044 mm/s (Richards et al. 2018), and 1410 °C mantle potential temperature

(Sarafian et al. 2017) with an adiabat slope after Katsura (2022). The peridotite/melt partition coefficients for water are parametrized following O'Leary et al. (2010). **(b)** The thermal model is the same as in **(a)**, but we used our preferred parametrization for the pyroxene/melt partition coefficients for water, and a constant value of 0.0013 for the olivine/melt partition coefficient (see Supplementary Information). **(c)** The partition coefficients are the same as in **(b)**, while the thermal structure of the oceanic lithosphere is described by the half-space cooling model (e.g. Schubert et al. 2001) with a 1333 °C mantle potential temperature (Richards et al. 2018). **(d)** The partition coefficients are the same as in **(b)** and **(c)**, and they are combined with the preferred thermal model of Richards et al. (2018) with a mantle potential temperature of 1333 °C and an adiabat slope (at depths > 138 km) after Katsura (2022)

compare how assuming different peridotite/melt partition coefficients may affect the model. We note that the values from O'Leary et al. (2010), which are used in Fig. 5a, are the highest proposed so far and that they limit the extent of melting in the model (Fig. 5a), relative to our preferred values (Fig. 5b; Supplementary Information). Estimates of the dry peridotite solidus also differ, and the model predictions shift when various literature sources are used in the calculation. In the supplementary Fig. S4b and S4c, we assumed the preferred dry solidi after Walter (1998) and Hirschmann (2000), respectively, which changed the predictions of water content required for incipient melting by up to 40 ppm. We also emphasize that the commonly accepted dry peridotite solidus (Hirschmann 2000) may in reality already be depressed due to atmospheric water contamination in starting materials (Sarafian et al. 2017), but it is not clear how this affects the model. The nominally dry solidus is used both in the parametrization of the ΔT - c_{H_2O} , and also in the melting model to obtain the difference between dry melting temperature and the geotherm (Supplementary Information), so the uncertainty related to the 'dry' solidus being 'damp' may mostly cancel out. The nominally dry solidus from our parametrization of the ΔT - c_{H_2O} is also defined by datapoints that are possibly 'damp' (Presnall et al. 1978), and the ΔT in Fig. 4 may eventually be corrected to higher values.

Nevertheless, our experiments show that hydrous partial melt is almost certainly present in extensive regions of the upper mantle beneath oceans (Fig. 5). Along a 50 Ma oceanic geotherm, the updated model predicts incipient mantle melting in equilibrium with approximately 80 to 220 ppm of water (Fig. 5). In comparison, initial calculations that relied on the previous ΔT - c_{H_2O} calibration (Hirschmann et al. 2009) required nearly 300 ppm of water to produce a melt, which exceeds most estimates of MORB source water contents (Michael 1988, 1995; Danyushevsky et al. 2000; Saal et al. 2002). Although the choice of the dry peridotite solidus and the mineral/melt partition coefficients for water has a significant effect on the model prediction, our calculations suggest that melt distribution and fractions are mostly controlled by the mantle potential temperature (Fig. 5b and c). Different studies have suggested a range of plausible mantle potential temperatures, from below 1300 to above 1450 °C (Sarafian et al. 2017; Richards et al. 2018 and ref. therein; Katsura 2022). In Fig. 5b and c, we assumed that the thermal structure of the oceanic lithosphere can be approximated by the half-space cooling model (e.g. Schubert et al. 2001) with mantle potential temperatures of 1410 and 1333 °C (Richards et al. 2018; Sarafian et al. 2017), while keeping other model parameters constant. At the higher end of suggested mantle potential temperatures, the model predicts relatively high melt fractions of several wt% in the youngest oceanic asthenosphere (Fig. 5a and b), which may be

overall consistent with observations of some magnetotelluric surveys (e.g. Naif et al. 2013). The melt fractions derived from S-wave velocity and attenuation in global tomographic models range up to 0.7 wt%, but are mostly below 0.4 wt%, throughout the oceanic low velocity zone (Debayle et al. 2020). For bulk water contents approaching 200 ppm, and assuming mantle potential temperature close to 1400 °C, the melting model also predicts similar melt fractions along the 50 and 75 Ma oceanic geotherms (Fig. 5a and b). Some partial melt may be stabilized in the young oceanic lithosphere even with a significantly lower mantle potential temperature of 1333 °C, but the predicted melt fractions are less than 0.1 wt% in this case (Fig. 5c). We then compared the half-space cooling model from Fig. 5c to a more realistic thermal structure of oceanic lithosphere that was proposed by Richards et al. (2018), which includes a crustal layer with low thermal conductivity, as well as pressure and temperature dependent thermal parameters for the lithosphere. This model has almost no age-dependence in terms of the predicted melt fractions (Fig. 5d). As a result, incipient melting may be possible with around 200 ppm of water, even in the oldest regions of the oceanic asthenosphere, and assuming a relatively low mantle potential temperature of 1333 °C.

We closely constrained the freezing point depression of basaltic melts with dissolved water contents of up to 5 wt% (Fig. 4), which is sufficient to model partial melting along most oceanic geotherms without the need to extrapolate the data considerably (Fig. 5). However, extrapolation of the melting point depression to higher melt water contents is necessary to predict melting in the subcontinental mantle. For melt water contents of 8 to 9 wt%, our extrapolations diverge from previous estimates by around 100 °C (Fig. 4), which should notably change the predictions of melt distribution beneath continents. We assumed that geotherms with surface heat flow of 50 to 40 mW/m² from the preferred geotherm family of Hasterok and Chapman (2011) generally encompass the thermal structure of the continental upper mantle. The results suggest that incipient melting may be possible in the hotter subcontinental regions in the presence of about 200 ppm of water, but we find that higher water contents of about 300 ppm may be required to stabilize melt along the 40 mW/m² geotherm (Supplementary Information, Fig. S5).

That is consistent with seismic surveys, as sharp discontinuities that are difficult to explain by temperature or compositional variations alone were reported regionally in the Phanerozoic subcontinental mantle by several studies (Rychert et al. 2020 and ref. therein). The existence of sharp discontinuities beneath cratons is less certain. Rychert et al. (2020) discuss how discontinuities are regularly imaged in cratonic regions by SS precursors, but only rarely by receiver functions. As the two methodologies have

different lateral resolutions, small-scale features along the lithosphere-asthenosphere boundary are a likely explanation. Interestingly, a recent study that combined magnetotelluric and seismic observations (Manassero et al. 2024) interpreted a series of conductive anomalies along the lithosphere-asthenosphere boundary in Southeast Australia. These anomalies were attributed to heterogeneously elevated water contents in the investigated region, probably exceeding the generally accepted upper limit of 200 ppm of water in the average MORB source. Provided this case study is broadly representative of the subcontinental mantle, the lithosphere-asthenosphere boundary beneath continents – particularly in the colder regions – may well be characterized by laterally discontinuous melt layers with partial melt being restricted to small-scale enrichment zones.

Conclusions

We used the anorthite-diopside- H_2O system to demonstrate a substantially greater effect of water on the freezing point depression of basaltic melts, as compared to earlier estimates. Our approach avoids most of the uncertainties inherent in previous studies, and the new data should allow much more accurate predictions of melt distribution in the upper mantle, as further constraints from experimental studies and geophysical surveys become available. We combined our measurements, which relate the near-solidus melt water contents (c_{H_2O}) to the corresponding freezing point depression (ΔT), with various literature sources to establish an improved hydrous melting model for the upper mantle. The results of the revised model differ, depending on choice of dry peridotite solidus and mineral/melt partition coefficient values. However, the predictions of melt distribution in the low velocity zone are particularly affected by differences in the assumed thermal structure of the lithosphere and uppermost asthenosphere. Regardless of the choice of other model parameters, the new ΔT - c_{H_2O} parametrization suggests that partial melting is possible with notably lower bulk water contents than previously thought. Even without any contribution to the freezing point depression by CO_2 , most variations of the model indicate that melt may be stable in the presence of about 200 ppm of water along extensive regions of the oceanic lithosphere-asthenosphere boundary, as well as in younger sections of the subcontinental mantle.

Supplementary Information The online version contains supplementary material available at <https://doi.org/10.1007/s00410-024-02177-2>.

Acknowledgements This study was supported by the German Science Foundation (DFG, GRK 2156). We acknowledge the support of T. Boffa Ballaran and D. Krauß during XRD and EPMA measurements, and we thank R. Njul for help with preparation of glass cylinders and

for sample polishing. Constructive comments from two anonymous reviewers improved the manuscript.

Funding Open Access funding enabled and organized by Projekt DEAL.

Data availability All relevant raw data for this study are included in the electronic supplementary material.

Open Access This article is licensed under a Creative Commons Attribution 4.0 International License, which permits use, sharing, adaptation, distribution and reproduction in any medium or format, as long as you give appropriate credit to the original author(s) and the source, provide a link to the Creative Commons licence, and indicate if changes were made. The images or other third party material in this article are included in the article's Creative Commons licence, unless indicated otherwise in a credit line to the material. If material is not included in the article's Creative Commons licence and your intended use is not permitted by statutory regulation or exceeds the permitted use, you will need to obtain permission directly from the copyright holder. To view a copy of this licence, visit <http://creativecommons.org/licenses/by/4.0/>.

References

- Adam J, Turner M, Hauri E, Turner S (2016) Crystal/melt partitioning of water and other volatiles during the near-solidus melting of mantle peridotite: comparisons with non-volatile incompatible elements and implications for the generation of intraplate magmatism. *Am Min* 101(4):876–888. <https://doi.org/10.2138/am-2016-5437>
- Anderson D, Sammis C (1969) The low velocity zone. *Geophys Int* 9:3–19
- Aubaud C, Hauri E, Hirschmann M (2004) Hydrogen partition coefficients between nominally anhydrous minerals and basaltic melts. *Geophys Res Lett* 31(20). <https://doi.org/10.1029/2004GL021341>
- Aubaud C, Hirschmann M, Withers A, Hervig R (2008) Hydrogen partitioning between melt, clinopyroxene, and garnet at 3 GPa in a hydrous MORB with 6 wt.% H_2O . *Contrib Mineral Petrol* 156(5):607–625. <https://doi.org/10.1007/s00410-008-0304-2>
- Bali E, Bolfan-Casanova N, Koga K (2008) Pressure and temperature dependence of H solubility in forsterite: an implication to water activity in the Earth Interior. *Earth Planet Sci Lett* 268(3–4):354–363. <https://doi.org/10.1016/j.epsl.2008.01.035>
- Balta J, Asimow P, Mosenfelder J (2011) Hydrous, low-carbon melting of garnet peridotite. *J Petrol* 52(11):2079–2105. <https://doi.org/10.1093/petrology/egr040>
- Bartholomew RF, Butler BL, Hoover HL, Wu CK (1980) Infrared spectra of a water-containing glass. *J Amer Ceramic Soc* 63:481–485. <https://doi.org/10.1111/j.1151-2916.1980.tb10748.x>
- Berndt J, Liebske C, Holtz F, Freise M, Nowak M, Ziegenbein D, Hurkuck W, Koepke J (2002) A combined rapid-quench and H_2 -membrane setup for internally heated pressure vessels: description and application for water solubility in basaltic melts. *Am Min* 87(11–12):1717–1726. <https://doi.org/10.2138/am-2002-11-1222>
- Botcharnikov R, Koepke J, Holtz F, McCammon C, Wilke M (2005) The effect of water activity on the oxidation and structural state of Fe in a ferro-basaltic melt. *Geochim Cosmochim Acta* 69(21):5071–5085. <https://doi.org/10.1016/j.gca.2005.04.023>
- Canil D (1990) Experimental study bearing on the absence of carbonate in mantle-derived xenoliths. *Geology* 18(10):1011–1013.

- [https://doi.org/10.1130/0091-7613\(1990\)018%3C1011:ESBOTA%3E2.3.CO;2](https://doi.org/10.1130/0091-7613(1990)018%3C1011:ESBOTA%3E2.3.CO;2)
- Cline C, Faul U, David E, Berry A, Jackson I (2018) Redox-influenced seismic properties of upper-mantle olivine. *Nature* 555(7696):355–358. <https://doi.org/10.1038/nature25764>
- Danyushevsky L, Eggins S, Falloon T, Christie D (2000) H₂O abundance in depleted to moderately enriched mid-ocean ridge magmas; part I: incompatible behaviour, implications for mantle storage, and origin of regional variations. *J Petrol* 41(8):1329–1364. <https://doi.org/10.1093/petrology/41.8.1329>
- De Yoreo J, Lange R, Navrotsky A (1995) Scanning calorimetric determinations of the heat contents of diopside-rich systems during melting and crystallization. *Geochim Cosmochim Acta* 59(13):2701–2707. [https://doi.org/10.1016/0016-7037\(95\)00166-W](https://doi.org/10.1016/0016-7037(95)00166-W)
- Debayle E, Bodin T, Durand S, Ricard Y (2020) Seismic evidence for partial melt below tectonic plates. *Nature* 586(7830):555–559. <https://doi.org/10.1038/s41586-020-2809-4>
- Demouchy S, Bolfan-Casanova N (2016) Distribution and transport of hydrogen in the lithospheric mantle: a review. *Lithos* 240–243:402–425. <https://doi.org/10.1016/j.lithos.2015.11.012>
- Dixon J, Stolper E, Holloway J (1995) An experimental study of water and carbon dioxide solubilities in mid-ocean ridge basaltic liquids. Part I: calibration and solubility models. *J Petrol* 36:1607–1631. <https://doi.org/10.1093/OXFORDJOURNALS.PETROLOGY.A037267>
- Dobson P, Skogby H, Rossman G (1995) Water in boninite glass and coexisting orthopyroxene: concentration and partitioning. *Contrib Mineral Petrol* 118(4):414–419. <https://doi.org/10.1007/s004100050023>
- Faul U, Jackson I (2005) The seismological signature of temperature and grain size variations in the upper mantle. *Earth Planet Sci Lett* 234:119–134. <https://doi.org/10.1016/J.EPSL.2005.02.008>
- Gaetani G, Grove T (1998) The influence of water on melting of mantle peridotite. *Contrib Mineral Petrol* 131:323–346. <https://doi.org/10.1007/S004100050396>
- Grant K, Kohn S, Brooker R (2007) The partitioning of water between olivine, orthopyroxene and melt synthesised in the system albite–forsterite–H₂O. *Earth Planet Sci Lett* 260(1–2):227–241. <https://doi.org/10.1016/j.epsl.2007.05.032>
- Green D (2015) Experimental petrology of peridotites, including effects of water and carbon on melting in the Earth's upper mantle. *Phys Chem Mineral* 42(2):95–122. <https://doi.org/10.1007/s00269-014-0729-2>
- Grove T, Chatterjee N, Parman S, Médard E (2006) The influence of H₂O on mantle wedge melting. *Earth Planet Sci Lett* 249:74–89. <https://doi.org/10.1016/j.epsl.2006.06.043>
- Hall L (1999) The effect of water on mantle melting. PhD thesis, Department of Earth Sciences, University of Bristol
- Hasterok D, Chapman D (2011) Heat production and geotherms for the continental lithosphere. *Earth Planet Sci Lett* 307(1–2):59–70. <https://doi.org/10.1016/j.epsl.2011.04.034>
- Hauri E, Gaetani G, Green T (2006) Partitioning of water during melting of the Earth's upper mantle at H₂O-undersaturated conditions. *Earth Planet Sci Lett* 248(3–4):715–734. <https://doi.org/10.1016/j.epsl.2006.06.014>
- Hirose K (1997) Melting experiments on lherzolite KLB-1 under hydrous conditions and generation of high-magnesian andesitic melts. *Geology* 25:42–44. [https://doi.org/10.1130/0091-7613\(1997\)025%3C0042:MEOLKU%3E2.3.CO;2](https://doi.org/10.1130/0091-7613(1997)025%3C0042:MEOLKU%3E2.3.CO;2)
- Hirose K, Kawamoto T (1995) Hydrous partial melting of lherzolite at 1 GPa: the effect of H₂O on the genesis of basaltic magmas. *Earth Planet Sci Lett* 133:463–473. [https://doi.org/10.1016/0012-821X\(95\)00096-U](https://doi.org/10.1016/0012-821X(95)00096-U)
- Hirschmann M (2000) Mantle solidus: experimental constraints and the effects of peridotite composition. *Geochem Geophys Geosyst* 1(10):2000GC000070. <https://doi.org/10.1029/2000GC000070>
- Hirschmann M (2010) Partial melt in the oceanic low velocity zone. *Phys Earth Planet Inter* 179:60–71. <https://doi.org/10.1016/J.PEPI.2009.12.003>
- Hirschmann M, Tenner T, Aubaud C, Withers A (2009) Dehydration melting of nominally anhydrous mantle: the primacy of partitioning. *Phys Earth Planet Inter* 176:54–68. <https://doi.org/10.1016/J.PEPI.2009.04.001>
- Hua J, Fischer K, Becker T, Gazel E, Hirth G (2023) Asthenospheric low-velocity zone consistent with globally prevalent partial melting. *Nat Geosci* 16(2):175–181. <https://doi.org/10.1038/s41561-022-01116-9>
- Karato S, Jung H (1998) Water, partial melting and the origin of the seismic low velocity and high attenuation zone in the upper mantle. *Earth Planet Sci Lett* 157:193–207. [https://doi.org/10.1016/S0012-821X\(98\)00034-X](https://doi.org/10.1016/S0012-821X(98)00034-X)
- Katsura T (2022) A revised adiabatic temperature profile for the mantle. *J Geophys Res* 127(2). <https://doi.org/10.1029/2021jb023562>
- Katz R, Spiegelman M, Langmuir C (2003) A new parameterization of hydrous mantle melting. *Geochem Geophys Geosyst* 4(9). <https://doi.org/10.1029/2002GC000433>
- Keppeler H, Bolfan-Casanova N (2006) Thermodynamics of water solubility and partitioning. *Rev Mineral Geochem* 62:193–230. <https://doi.org/10.1515/9781501509476-013>
- Keppeler H, Rauch M (2000) Water solubility in nominally anhydrous minerals measured by FTIR and ¹H MAS NMR: the effect of sample preparation. *Phys Chem Mineral* 27(6):371–376. <https://doi.org/10.1007/s002699900070>
- Koga K, Hauri E, Hirschmann M, Bell D (2003) Hydrogen concentration analyses using SIMS and FTIR: comparison and calibration for nominally anhydrous minerals. *Geochem Geophys Geosyst* 4(2). <https://doi.org/10.1029/2002GC000378>
- Lange R, De Yoreo J, Navrotsky A (1991) Scanning calorimetric measurement of heat capacity during incongruent melting of diopside. *Am Min* 76:904–912
- Le Voyer M, Asimow P, Mosenfelder J, Guan Y, Wallace P, Schiano P, Stolper E, Eiler J (2014) Zonation of H₂O and F concentrations around melt inclusions in olivines. *J Petrol* 55(4):685–707. <https://doi.org/10.1093/petrology/egu003>
- Le Voyer M, Kelley K, Cottrell E, Hauri E (2017) Heterogeneity in mantle carbon content from CO₂-undersaturated basalts. *Nat Comms* 8(1). <https://doi.org/10.1038/ncomms14062>
- Lesne P, Scaillet B, Pichavant M, Iacono-Marziano G, Beny JM (2011) The H₂O solubility of alkali basaltic melts: an experimental study. *Contrib Mineral Petrol* 162:133–151. <https://doi.org/10.1007/s00410-010-0588-x>
- Litasov K, Ohtani E, Kagi H, Jacobsen S, Ghosh S (2007) Temperature dependence and mechanism of hydrogen incorporation in olivine at 12.5–14.0 GPa. *Geophys Res Lett* 34(16). <https://doi.org/10.1029/2007GL030737>
- Manassero M, Özaydın S, Afonso J, Shea J, Ezad I, Kirkby A, Thiel S, Fomin I, Czarnota K (2024) Lithospheric structure and melting processes in Southeast Australia: new constraints from joint probabilistic inversions of 3D magnetotelluric and seismic data. *J Geophys Res Solid Earth* 129(3). <https://doi.org/10.1029/2023JB028257>
- Matsuno T, Seama N, Evans R, Chave A, Baba K, White A, Goto T, Heinson G, Boren G, Yoneda A, Utada H (2010) Upper mantle electrical resistivity structure beneath the central Mariana subduction system. *Geochem Geophys Geosyst* 11(9). <https://doi.org/10.1029/2010GC003101>
- Michael P (1988) The concentration, behavior and storage of H₂O in the suboceanic upper mantle: implications for

- mantle metasomatism. *Geochim Cosmochim Acta* 52(2):555–566. [https://doi.org/10.1016/0016-7037\(88\)90110-X](https://doi.org/10.1016/0016-7037(88)90110-X)
- Michael P (1995) Regionally distinctive sources of depleted MORB: evidence from trace elements and H₂O. *Earth Planet Sci Lett* 131:301–320. [https://doi.org/10.1016/0012-821X\(95\)00023-6](https://doi.org/10.1016/0012-821X(95)00023-6)
- Mierdel K, Keppler H, Smyth J, Langenhorst F (2007) Water solubility in aluminous orthopyroxene and the origin of Earth's asthenosphere. *Science* 315(5810):364–368. <https://doi.org/10.1126/science.1135422>
- Naif S, Key K, Constable S, Evans R (2013) Melt-rich channel observed at the lithosphere–asthenosphere boundary. *Nature* 495(7441):356–359. <https://doi.org/10.1038/nature11939>
- Newcombe M, Plank T, Barth A, Asimow P, Hauri E (2020) Water-in-olivine magma ascent chronometry: every crystal is a clock. *J Volcanol Geotherm Res* 398:106872. <https://doi.org/10.1016/j.jvolgeores.2020.106872>
- Nowak M, Behrens H (1995) The speciation of water in haplogranitic glasses and melts determined by in situ near-infrared spectroscopy. *Geochim Cosmochim Acta* 59:3445–3450. [https://doi.org/10.1016/0016-7037\(95\)00237-T](https://doi.org/10.1016/0016-7037(95)00237-T)
- O'Leary J, Gaetani G, Hauri E (2010) The effect of tetrahedral Al³⁺ on the partitioning of water between clinopyroxene and silicate melt. *Earth Planet Sci Lett* 297(1–2):111–120. <https://doi.org/10.1016/j.epsl.2010.06.011>
- Ohlhorst S, Behrens H, Holtz F (2001) Compositional dependence of molar absorptivities of near-infrared OH⁻ and H₂O bands in rhyolitic to basaltic glasses. *Chem Geol* 174(1–3):5–20. [https://doi.org/10.1016/S0009-2541\(00\)00303-X](https://doi.org/10.1016/S0009-2541(00)00303-X)
- Osborn E (1942) The system CaSiO₃–diopside–anorthite. *Am J Sci* 240(11):751–788. <https://doi.org/10.2475/ajs.240.11.751>
- Presnall D, Dixon S, Dixon J, O'Donnell T, Brenner N, Schrock R, Dycus D (1978) Liquidus phase relations on the join diopside–forsterite–anorthite from 1 atm to 20 kbar: their bearing on the generation and crystallization of basaltic magma. *Contrib Mineral Petrol* 66:203–220. <https://doi.org/10.1007/BF00372159>
- Putak Juriček M, Keppler H (2023) Amphibole stability, water storage in the mantle, and the nature of the lithosphere–asthenosphere boundary. *Earth Planet Sci Lett* 608:118082. <https://doi.org/10.1016/j.epsl.2023.118082>
- Raoult F-M (1882) Loi générale de congélation des dissolvants (General law of the freezing of solvents). *Comptes Rendus* 95:1030–1033
- Richards F, Hoggard M, Cowton L, White N (2018) Reassessing the thermal structure of oceanic lithosphere with revised global inventories of basement depths and heat flow measurements. *J Geophys Res* 123(10):9136–9161. <https://doi.org/10.1029/2018jb015998>
- Richet P, Bottinga Y (1984) Anorthite, andesine, wollastonite, diopside, cordierite and pyrope: thermodynamics of melting, glass transitions, and properties of the amorphous phases. *Earth Planet Sci Lett* 67:415–432. [https://doi.org/10.1016/0012-821X\(84\)90179-1](https://doi.org/10.1016/0012-821X(84)90179-1)
- Rychert C, Harmon N, Constable S, Wang S (2020) The nature of the lithosphere–asthenosphere boundary. *J Geophys Res Solid Earth* 125(10). <https://doi.org/10.1029/2018JB016463>
- Saal A, Hauri E, Langmuir C, Perfit M (2002) Vapour undersaturation in primitive mid-ocean-ridge basalt and the volatile content of Earth's upper mantle. *Nature* 419:451–455. <https://doi.org/10.1038/nature01073>
- Sakamaki T, Ohtani E, Urakawa S, Suzuki A, Katayama Y (2009) Measurement of hydrous peridotite magma density at high pressure using the X-ray absorption method. *Earth Planet Sci Lett* 287:293–297. <https://doi.org/10.1016/j.epsl.2009.07.030>
- Sarafian E, Gaetani G, Hauri E, Sarafian A (2017) Experimental constraints on the damp peridotite solidus and oceanic mantle potential temperature. *Science* 355(6328):942–945. <https://doi.org/10.1126/science.aaj2165>
- Schubert G, Turcotte D, Olson P (2001) *Mantle Convection in the Earth and planets*. Cambridge University Press, Cambridge
- Shcheka S, Wiedenbeck M, Frost D, Keppler H (2006) Carbon solubility in mantle minerals. *Earth Planet Sci Lett* 245(3–4):730–742. <https://doi.org/10.1016/j.epsl.2006.03.036>
- Shen A, Keppler H (1995) Infrared spectroscopy of hydrous silicate melts to 1000°C and 10 kbar: direct observation of H₂O speciation in a diamond-anvil cell. *Am Min* 80:1335–1338. <https://doi.org/10.2138/am-1995-11-1223>
- Shishkina T, Botcharnikov R, Holtz F, Almeev R, Portnyagin M (2010) Solubility of H₂O- and CO₂-bearing fluids in tholeiitic basalts at pressures up to 500 MPa. *Chem Geol* 277:115–125. <https://doi.org/10.1016/J.CHEMGEO.2010.07.014>
- Smyth J, Frost D, Nestola F, Holl C, Bromiley G (2006) Olivine hydration in the deep upper mantle: effects of temperature and silica activity. *Geophys Res Lett* 33(15). <https://doi.org/10.1029/2006GL026194>
- Stebbins J (1995) Dynamics and structure of silicate and oxide melts; nuclear magnetic resonance studies. *Rev Mineral Geochem* 32:191–246
- Stolper E (1982) The speciation of water in silicate melts. *Geochim Cosmochim Acta* 46:2609–2620. [https://doi.org/10.1016/0016-7037\(82\)90381-7](https://doi.org/10.1016/0016-7037(82)90381-7)
- Takei Y (2017) Effects of partial melting on seismic velocity and attenuation: a new insight from experiments. *Annu Rev Earth Planet Sci* 45(1):447–470. <https://doi.org/10.1146/annurev-earth-063016-015820>
- Tenner T, Hirschmann M, Withers A, Hervig R (2009) Hydrogen partitioning between nominally anhydrous upper mantle minerals and melt between 3 and 5 GPa and applications to hydrous peridotite partial melting. *Chem Geol* 262:42–56. <https://doi.org/10.1016/J.CHEMGEO.2008.12.006>
- Tenner T, Hirschmann M, Humayun M (2012) The effect of H₂O on partial melting of garnet peridotite at 3.5 GPa. *Geochem Geophys Geosyst* 13(3). <https://doi.org/10.1029/2011GC003942>
- Tuttle O, England J (1955) Preliminary report on the system SiO₂–H₂O. *Geol Soc Am Bull* 66(1):149–152. [https://doi.org/10.1130/0016-7606\(1955\)66\[149:PROTSS\]2.0.CO;2](https://doi.org/10.1130/0016-7606(1955)66[149:PROTSS]2.0.CO;2)
- Walter M (1998) Melting of garnet peridotite and the origin of komatiite and depleted lithosphere. *J Petrol* 39(1):29–60. <https://doi.org/10.1093/ptro/39.1.29>
- Wang S, Constable S, Rychert C, Harmon N (2020) A lithosphere–asthenosphere boundary and partial melt estimated using marine magnetotelluric data at the Central Middle Atlantic Ridge. *Geochem Geophys Geosyst* 21(9). <https://doi.org/10.1029/2020GC009177>
- Withers A, Hirschmann M (2008) Influence of temperature, composition, silica activity and oxygen fugacity on the H₂O storage capacity of olivine at 8 GPa. *Contrib Mineral Petrol* 156(5):595–605. <https://doi.org/10.1007/s00410-008-0303-3>
- Yoder H (1965) Diopside–anorthite–water at five and ten kilobars and its bearing on explosive volcanism. *Carnegie Institution Year Book* 64:82–89

Publisher's note Springer Nature remains neutral with regard to jurisdictional claims in published maps and institutional affiliations.